PHYSICAL REVIEW A VOLUME 52, NUMBER 2 AUGUST 1995

Probe transmission in a two-dimensional optical lattice

J. Guo
Joint Institute for Laboratory Astrophysics, University of Colorado, Boulder, Colorado 80309-0440

(Received 9 January 1995)

We present a calculation of the probe-transmission spectrum of a two-dimensional optical lattice, in which atoms are cooled by a pair of standing-wave fields with perpendicular polarizations within the plane of incidence. A probe laser is directed along the axis of one of the cooling fields, with a polarization parallel to the incident plane of the cooling fields. The calculated probe-transmission spectrum exhibits both sidebands, which originate from stimulated Raman transitions between different vibrational states of the atoms in the molasses, and a central resonance structure, which originates from Rayleigh resonances among these vibrational states. We also include in our calculation a possible misalignment of the probe field relative to the axis of the cooling field. It is shown that the effects of the probe misalignment can lead to significant modifications to the central resonance signal.

PACS number(s): 32.80.Pj, 42.65.−k

I. INTRODUCTION

In a normal optical molasses, atoms are cooled by a number of incident fields whose polarizations are orthogonal to each other. The equilibrium energy of the cooled atoms can be sufficiently small, such that these atoms can become spatially localized at the minima of the light-induced potential wells, and form a spatial lattice structure, i.e., optical lattices. The dynamics of the cold atoms trapped in the light-induced potentials can be studied by pump-probe techniques, such as probe transmission or four-wave mixing spectroscopy. In these types of experiments, the cooling fields also play the role of the pump fields. Some early experiments in one-dimensional (1D) molasses [1,2] provided direct evidence of the quantization of the atomic motion in the molasses. Recently, both probe-transmission [3–5] and four-wave mixing [6] experiments were carried out in 2D and 3D molasses, and the obtained spectra in these experiments exhibit rich and sometimes unexpected features.

On the theoretical side, qualitative understanding of the spectroscopy of the optical lattices is still at the beginning. Calculations of the probe-transmission or four-wave mixing signals in 1D molasses [7,8] have been published recently, and good agreement between the calculations and the experimental results have been achieved. Up till now, however, a rigorous theoretical investigation on the spectroscopy of 2D or 3D molasses did not exist, partially owing to the fact that a calculation similar to those in Refs. [7,8] proved to be much more difficult and computationally demanding in higher dimensions.

In this paper, we calculate the probe-transmission spectrum of a 2D optical molasses. As shown in Fig. 1, the cooling field having a frequency ω consists of a pair of standing-wave fields along the x and y axes, polarized in the y and x directions, respectively. A probe field of frequency ω' is incident along the x direction, with a polarization in the y direction. In our calculation, we allow a small misalignment between the propagation directions of the probe and the cooling fields denoted by a small angle θ. Theoretical investigations of Sisyphus cooling in the same 2D configuration have been carried out both semi-classically [9–11] and fully quantum mechanically [12,13]. It was shown [9–11] that cooling in this situation depends sensitively on the relative phase $\delta\phi$ between the two standing-wave fields. In this calculation, we assume that $\delta\phi$ is fixed at $\pi/2$, which leads to maximum cooling effects. The atomic level scheme is assumed to be a $J_g = 1/2 \rightarrow J_e = 3/2$ transition. Similar to an earlier 1D calculation [8], we also investigate the effects related to a possible misalignment of the probe field relative to the propagation of the cooling field both within and outside of the molasses plane. We show that the probe misalignment can result in significant modifications to a central resonance signal in the calculated spectrum.

This paper is organized as follows. In Sec. II, we write down the Hamiltonian for the system under investigation and the master equation governing the evolution of the atomic density matrix. In Sec. III, a Bloch-state basis is introduced, in which the atomic density matrix is expanded and solved under a secular approximation. Then in Sec. IV, we calculate the probe-transmission spectrum

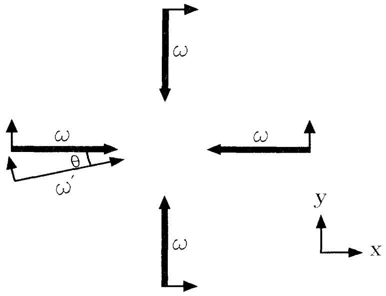

FIG. 1. Cooling and probing field configuration of a 2D optical lattice.

of this 2D lattice, assuming that the probe field is propagating exactly along the x axis. In Sec. V, the effects related to the misalignment of the probe field are analyzed. We conclude in Sec. VI by discussing the relation of our calculation to some existing experiments.

II. DENSITY MATRIX EQUATION AND THE BLOCH-STATE BASIS

The incident fields shown in Fig. 1 can be written explicitly as

$$\mathbf{E} = \frac{1}{2}\mathcal{E}e^{-i\omega t}(\cos kx\hat{\mathbf{y}} - i\cos ky\hat{\mathbf{x}} + \epsilon e^{i\mathbf{k}'\cdot\mathbf{r}-i\delta t}\hat{\mathbf{y}}) + \text{c.c.}\,, \tag{1}$$

where ω is the cooling field frequency, $\mathbf{k}'$ is the probe field wave vector, $\delta = \omega' - \omega$ is the detuning between the probe field and the cooling field, and the constant ϵ is the ratio between the magnitudes of the probe and cooling fields, assumed to be much smaller than unity.

Throughout this calculation, we assume a limit of weak incident fields, which is appropriate for polarization gradient cooling. The weak-field limit is defined as

$$\chi \ll \Gamma, |\Delta|\,, \tag{2}$$

where $\chi = -d_{eg}\mathcal{E}/2\sqrt{2}\hbar$ is the cooling field Rabi frequency, Γ is the atomic excited state decay rate, and $\Delta = \omega - \omega_0$ is the cooling field detuning from the Bohr frequency ω_0 of the electronic transition. Under the weak-field limit, one can adiabatically eliminate the electronic excited states of the atoms, and derive an effective Hamiltonian for the electronic ground states of the atoms only. The resulting density matrix equation for the atoms is given by

$$\dot{\rho} = \frac{1}{i\hbar}[H, \rho] + [\dot{\rho}]_{\text{relax}}\,, \tag{3}$$

where the effective Hamiltonian H is given by

$$H = H^{(0)} + \epsilon[H^{(1)}e^{i\delta t} + \text{H.c.}]\,. \tag{4}$$

The zeroth-order term in Eq. (4), $H^{(0)}$, describes the motion of the atoms in the 2D periodic potential induced by the cooling field. It is given by

$$\begin{aligned} H^{(0)} = \frac{\mathbf{p}^2}{2M} &+ \frac{U_0}{3}(\cos^2 kx + \cos^2 ky \\ &+ \cos kx\cos ky)|+\rangle\langle+| \\ &+ \frac{U_0}{3}(\cos^2 kx + \cos^2 ky \\ &- \cos kx\cos ky)|-\rangle\langle-|\,, \end{aligned} \tag{5}$$

where $|\pm\rangle = |g \pm 1/2\rangle$, are the two magnetic sublevels of the atomic ground state, and U_0 is the depth of the light-induced potential wells, given by

$$U_0 = \frac{4\hbar\Delta|\chi|^2}{(\Gamma/2)^2 + \Delta^2}\,. \tag{6}$$

The first-order term in Eq. (4), $H^{(1)}$, is the modification to the light-shift potential introduced by the addition of the probe field. It is given by

$$\begin{aligned} H^{(1)} &= \frac{U_0}{3}(\cos kx + \tfrac{1}{2}\cos ky)e^{-i\mathbf{k}'\cdot\mathbf{r}}|+\rangle\langle+| \\ &\quad + \frac{U_0}{3}(\cos kx - \tfrac{1}{2}\cos ky)e^{-i\mathbf{k}'\cdot\mathbf{r}}|-\rangle\langle-|\,. \end{aligned} \tag{7}$$

The term $[\dot{\rho}]_{\text{relax}}$ in Eq. (3) denotes the relaxation of the atomic density matrix due to optical pumping induced by both the cooling and probe fields. For the $J_g = 1/2 \to J_e = 3/2$ transition considered in this calculation, the optical pumping term $[\dot{\rho}]_{\text{relax}}$ has a particularly simple form [13], and can be explicitly written out as

$$\begin{aligned} [\dot{\rho}]_{\text{relax}} = &-\frac{\Gamma'}{2}[A\rho + \rho A] + \Gamma'\int d\mathbf{p}' \\ &\times \sum_{Q=-1}^{1} N_Q(\mathbf{p}')B_Q^{\dagger}e^{-i\mathbf{p}'\cdot\mathbf{r}}\rho e^{i\mathbf{p}'\cdot\mathbf{r}}B_Q\,, \end{aligned} \tag{8}$$

where

$$\Gamma' = \frac{\Gamma|\chi|^2}{(\Gamma/2)^2 + \Delta^2} \tag{9}$$

is the optical pumping rate. The operators A and B_Q in Eq. (8) can be written as

$$\begin{aligned} A &= A^{(0)} + \epsilon[A^{(1)}e^{i\delta t} + \text{H.c.}]\,, \\ B_Q &= B_Q^{(0)} + \epsilon[B_Q^{(1)}e^{i\delta t} + \text{H.c.}]\,, \end{aligned} \tag{10}$$

where

$$\begin{aligned} A^{(0)} &= \frac{4}{3}(\cos^2 kx + \cos^2 ky + \cos kx\cos ky)|+\rangle\langle+| \\ &\quad + \frac{4}{3}(\cos^2 kx + \cos^2 ky \\ &\quad - \cos kx\cos ky)|-\rangle\langle-|\,, \\ A^{(1)} &= \frac{4}{3}(\cos kx + \tfrac{1}{2}\cos ky)e^{-i\mathbf{k}'\cdot\mathbf{r}}|+\rangle\langle+| \\ &\quad + \frac{4}{3}(\cos kx - \tfrac{1}{2}\cos ky)e^{-i\mathbf{k}'\cdot\mathbf{r}}|-\rangle\langle-|\,, \end{aligned} \tag{11}$$

and

$$\begin{aligned} B_{\pm1}^{(0)} &= (-i)(\cos kx \pm \cos ky)(|\pm\rangle\langle\pm| + \tfrac{1}{3}|\mp\rangle\langle\mp|)\,, \\ B_0^{(0)} &= (-i)\frac{\sqrt{2}}{3}[(\cos kx + \cos ky)|-\rangle\langle+| \\ &\quad + (\cos kx - \cos ky)|+\rangle\langle-|]\,, \\ B_{\pm1}^{(1)} &= (-i)e^{-i\mathbf{k}'\cdot\mathbf{r}}(|\pm\rangle\langle\pm| + \tfrac{1}{3}|\mp\rangle\langle\mp|)\,, \\ B_0^{(1)} &= (-i)e^{-i\mathbf{k}'\cdot\mathbf{r}}\frac{\sqrt{2}}{3}(|-\rangle\langle+| + |+\rangle\langle-|)\,. \end{aligned} \tag{12}$$

The kernels $N_Q(\mathbf{p}')$ in Eq. (8) are the probability distribution functions for the emission of a spontaneous photon having a spherical polarization component Q and a momentum $\hbar\mathbf{p}'$. The exact expressions for $N_Q(\mathbf{p}')$ can be derived based on a procedure described in details in Ref. [13]. In practice, one discretizes the spontaneous photon momentum $\hbar\mathbf{p}'$. Depending on the discretization scheme, the functions $N_Q(\mathbf{p}')$ can have different forms, examples of which will be described below.

The atomic density matrix can be written as

$$\rho = \rho^{(0)} + \epsilon\{\rho^{(1)}e^{i\delta t} + [\rho^{(1)}]^{\dagger}e^{-i\delta t}\} , \tag{13}$$

where $\rho^{(0)}$ is the steady-state density matrix in the absence of the probe field, and $\rho^{(1)}$ is the probe-induced modification to ρ. The probe transmission coefficient G_p can be found in terms of $\rho^{(1)}$ as [7]

$$G_p = \mathrm{Im}\left[\frac{\chi}{i\Gamma/2-\Delta}\langle\rho^{(1)}[(2\cos kx + \cos ky)e^{i\mathbf{k}'\cdot\mathbf{r}}|+\rangle\langle+| \right.$$
$$\left. +(2\cos kx - \cos ky)e^{i\mathbf{k}'\cdot\mathbf{r}}|-\rangle\langle-|]\rangle\right] . \tag{14}$$

III. BLOCH-STATE BASIS AND THE RATE EQUATIONS

The density matrix ρ can be solved in a so-called Bloch-state basis [12,13]. The Bloch states are the eigenstates of the Hamiltonian $H^{(0)}$, which describes the motion of the atoms in the light-induced 2D potential. They can be denoted as $|n,\mathbf{q},\epsilon\rangle$, where n is the energy band index, $\mathbf{q}$ is the Bloch index, and $\epsilon = \pm$ represents the two magnetic sublevels $|\pm\rangle$. In the position representation, the Bloch states can be expanded as

$$\langle\mathbf{r}|n,\mathbf{q},\epsilon\rangle = e^{i\mathbf{q}\cdot\mathbf{r}}\sum_{l,m=-N}^{N} \times C_{n,\mathbf{q},\epsilon}(l,m)e^{i(l+m)kx+i(l-m)ky} , \tag{15}$$

where $C_{n,\mathbf{q},\epsilon}(l,m)$ is the expansion coefficient and N is the cutoff value for the plane-wave components of the Bloch states. The maximum momentum component along either the x or y direction is limited to $2N\hbar k$. In the calculation below, N is chosen as $N \leq N_{\max} = 7$ [14]. The Bloch vector $\mathbf{q}$ can be chosen within the first Brillouin zone, which in this case is given by [12]

$$|q_x| + |q_y| \leq k . \tag{16}$$

In Fig. 2, we plot the energies of the Bloch states $|n,\mathbf{q},\pm\rangle$ as a function of the Bloch index $\mathbf{q} = q_y\hat{\mathbf{y}}$. Among the lowest Bloch states, there exists quasidegeneracy among certain Bloch states, which form an energy manifold. The degree of degeneracy, or the number of states in a manifold, increases linearly with energy, similar to the case of a 2D harmonic oscillator. This result is expected, since the lowest motional states are localized in the vicinity of the antinodes of the field, where the light-shift potential can be approximated by a 2D harmonic potential For highly excited Bloch states, on the other hand, the energy-momentum relation resembles that of free particles, with the exception of the existence of small energy gaps whenever two curves cross each other. The increase of the number of motional states with energy is absent in the 1D cases [15,16], and as we see below, such a property can lead to a substantial difference in the probe spectra between 1D and 2D cases.

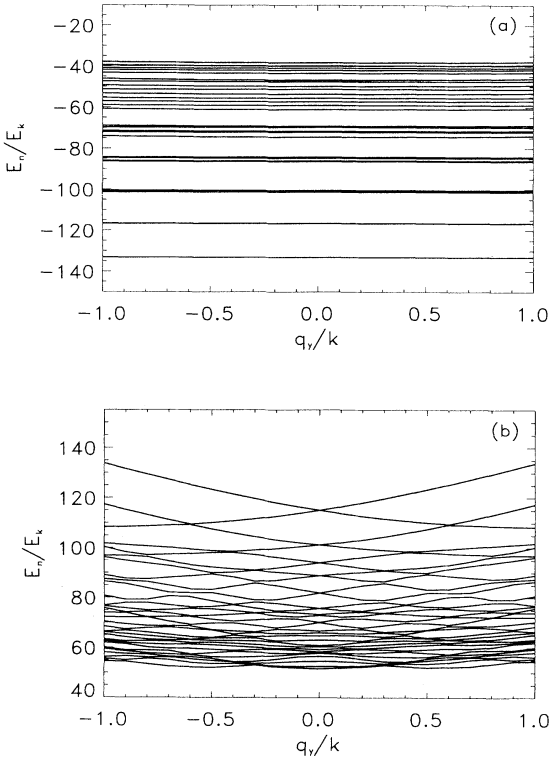

FIG. 2. The energy spectrum of atoms in the 2D potential. The potential depth $U_0 = -150E_k$. (a) The lowest 30 energy bands ($n = 0, 1, \ldots, 29$), and (b) the highest 30 bands ($n = 195, 196, \ldots, 224$).

To calculate the zeroth-order density matrix $\rho^{(0)}$, we invoke a secular approximation, which amounts to neglecting the off-diagonal density matrix elements between Bloch states with different energies. Such an approximation is valid for laser detunings much greater than the natural linewidth of the electronic transition [13], i.e.,

$$|\Delta| \gg \Gamma . \tag{17}$$

For the simple $J_g = 1/2 \to J_e = 3/2$ transition chosen in this calculation, and for the incident field configuration, the zeroth-order density matrix $\rho^{(0)}$ is diagonal in the Bloch-state basis [13]. Under the secular limit (17), the populations of various Bloch states

$$\pi_{n,\mathbf{q},\epsilon} = \langle n,\mathbf{q},\epsilon|\rho^{(0)}|n,\mathbf{q},\epsilon\rangle , \tag{18}$$

can be solved from the following rate equations:

$$\dot{\pi}_{n,\mathbf{q},\epsilon} = -\gamma_{n,\mathbf{q},\epsilon}\pi_{n,\mathbf{q},\epsilon} + \sum_{n',\mathbf{q}',\epsilon'}\gamma(n',\mathbf{q}',\epsilon';n,\mathbf{q},\epsilon)\pi_{n',\mathbf{q}',\epsilon'} , \tag{19}$$

where

$$\gamma_{n,\mathbf{q},\epsilon} = \langle n, \mathbf{q}, \epsilon | A^{(0)} | n, \mathbf{q}, \epsilon \rangle \,,$$

$$\gamma(n', \mathbf{q}', \epsilon'; n, \mathbf{q}, \epsilon)$$

$$= \int d\mathbf{p}' \sum_{Q} N_Q(\mathbf{p}') |\langle n', \mathbf{q}', \epsilon' | B_Q^{(0)} e^{i\mathbf{p}'\cdot\mathbf{r}} | n, \mathbf{q}, \epsilon \rangle|^2 \,. \tag{20}$$

The choice of the discretization scheme for the Bloch vectors $\mathbf{q}$ depends on the incident field configuration. For example, in the absence of the probe field, or if the probe field propagates exactly along the axis of the cooling field, one can choose a minimum number of Bloch vectors, as in the case of Refs. [12,13]. However, when the probe field propagates at a small angle with respect to the cooling laser axis, as we study below, one needs to choose a different set of Bloch vectors to resolve the grating structures excited by the addition of the probe field.

Similar to the 1D case [15], the steady-state values of the populations $\pi_{n,\mathbf{q},\epsilon}$ solved from Eq. (19) depends only on the reduced potential depth (U_0/E_k), where $E_k = \hbar^2 k^2 / 2M$ is the recoil energy. A detailed description of the properties of $\pi_{n,\mathbf{q},\epsilon}$ can be found in Refs. [12,13]. In particular, it is found that in the secular limit, there exist resonance peaks in the populations of the lowest Bloch states for certain values of U_0, and the appearances of such resonances have been attributed to the avoided crossings of the energy curves associated with a few motional states [12], and are found to smooth away in the nonsecular limit of smaller values of $|\Delta|/\Gamma$ [13].

IV. PROBE TRANSMISSION SPECTRUM IN THE ABSENCE OF PROBE MISALIGNMENT

After the solution for $\rho^{(0)}$ is obtained, one can solve for the first-order density matrix $\rho^{(1)}$ by substituting $\rho^{(0)}$ into Eq. (3). The evolution equation for $\rho^{(1)}$ is given by

$$\begin{aligned}\dot{\rho}^{(1)} = {} & \frac{1}{i\hbar}([H^{(0)}, \rho^{(1)}] + [H^{(1)}, \rho^{(0)}]) \\ & - \frac{\Gamma'}{2}[A^{(0)}\rho^{(1)} + \rho^{(1)}A^{(0)} + A^{(1)}\rho^{(0)} + \rho^{(0)}A^{(1)}] \\ & + \Gamma' \int d\mathbf{p}' \sum_{Q} N_Q(\mathbf{p}') [(B_Q^{(0)})^\dagger e^{-i\mathbf{p}'\cdot\mathbf{r}} \rho^{(1)} e^{i\mathbf{p}'\cdot\mathbf{r}} B_Q^{(0)} \\ & + (B_Q^{(0)})^\dagger e^{-i\mathbf{p}'\cdot\mathbf{r}} \rho^{(0)} e^{i\mathbf{p}'\cdot\mathbf{r}} B_Q^{(1)}] \,. \end{aligned} \tag{21}$$

The density matrix $\rho^{(1)}$ can be expanded in the Bloch-state basis as well, and the resulting expansion terms are denoted as

$$\rho^{(1)}(n, \mathbf{q}, \epsilon; n', \mathbf{q}', \epsilon) = \langle n, \mathbf{q}, \epsilon | \rho^{(1)} | n, \mathbf{q}', \epsilon \rangle \,. \tag{22}$$

In this section, we assume that the probe field propagates exactly along the x axis, with a polarization along the y axis. As a result, the first-order density matrix elements $\rho^{(1)}(n, \mathbf{q}, \epsilon; n', \mathbf{q}', \epsilon)$ with $\mathbf{q} \neq \mathbf{q}'$ vanish. To reduce the number of density matrix elements, we choose two Bloch indices

$$\mathbf{q} = -k\hat{\mathbf{x}} \,, \mathbf{0} \,, \tag{23}$$

and the simplified spontaneous emission kernels in Eq. (8) are described in the Appendix.

As shown in the previous section, in this case of 2D lattice, there exists quasidegeneracy of the Bloch states belonging to the lowest energy manifolds. For a finite value of $|\Delta|/\Gamma$ (e.g., less than 100), the energy separations between the states in these manifolds are much smaller than Γ', and in practice these states can be treated as exactly degenerate. We calculate the first-order terms $\rho^{(1)}(n, \mathbf{q}, \epsilon; n', \mathbf{q}, \epsilon)$ as follows.

First, the first-order density matrix elements with $n \neq n'$ represent a contribution to the signal due to stimulated Raman-type transitions between Bloch states of different energy bands. For the lowest few energy manifolds, in each of which the energy separations between the Bloch states are much smaller than Γ', the equations for the steady-state density matrix elements can be derived from Eq. (21) as

$$\begin{aligned} & -[\tfrac{1}{2}(\gamma_{n,\mathbf{q},\epsilon} + \gamma_{n',\mathbf{q},\epsilon}) + i\delta + i\omega_{n,\mathbf{q},\epsilon;n',\mathbf{q},\epsilon}]\rho^{(1)}(n, \mathbf{q}, \epsilon; n', \mathbf{q}, \epsilon) + \Gamma' \sum_{n'', n''', \mathbf{q}', \epsilon'} \int \sum_{Q} N_Q(\mathbf{p}') \\ & \qquad \times \langle n, \mathbf{q}, \epsilon | (B_Q^{(0)})^\dagger e^{-i\mathbf{p}'\cdot\mathbf{r}} | n'', \mathbf{q}', \epsilon' \rangle \langle n''', \mathbf{q}', \epsilon' | e^{i\mathbf{p}'\cdot\mathbf{r}} B_Q^{(0)} | n', \mathbf{q}, \epsilon \rangle \rho^{(1)}(n'', \mathbf{q}', \epsilon'; n''', \mathbf{q}', \epsilon') \\ & \qquad = \frac{i}{\hbar} \langle n, \mathbf{q}, \epsilon | H^{(1)} | n', \mathbf{q}, \epsilon \rangle (\pi_{n',\mathbf{q},\epsilon} - \pi_{n,\mathbf{q},\epsilon}) + \frac{\Gamma'}{2} \langle n, \mathbf{q}, \epsilon | A^{(1)} | n', \mathbf{q}, \epsilon \rangle (\pi_{n,\mathbf{q},\epsilon} + \pi_{n',\mathbf{q},\epsilon}) \\ & \qquad \quad - \Gamma' \sum_{n'', \mathbf{q}', \epsilon'} \int d\mathbf{p}' \sum_{Q} N_Q(\mathbf{p}') \langle n, \mathbf{q}, \epsilon | (B_Q^{(0)})^\dagger e^{-i\mathbf{p}'\cdot\mathbf{r}} | n'', \mathbf{q}', \epsilon' \rangle \\ & \qquad \quad \times \langle n'', \mathbf{q}', \epsilon' | e^{i\mathbf{p}'\cdot\mathbf{r}} B_Q^{(1)} | n', \mathbf{q}, \epsilon \rangle \pi_{n'',\mathbf{q}',\epsilon'} \,, \end{aligned} \tag{24}$$

where

$$\omega_{n,\mathbf{q},\epsilon;n',\mathbf{q},\epsilon} = \frac{1}{\hbar}(E_{n,\mathbf{q},\epsilon} - E_{n',\mathbf{q},\epsilon}) , \qquad (25)$$

is the frequency difference between two Bloch states $|n,\mathbf{q},\epsilon\rangle$ and $|n',\mathbf{q}',\epsilon\rangle$. In the above equation, the band indices n and n'' belong to the same energy manifold, while n' and n''' to a different manifold. For higher energy manifolds, the energy separations between different Bloch states becomes greater than the relaxtion rates of these Bloch states, owing to the anharmonicity of the light-shift potential. As a result, one can neglect the couplings between the coherences $\rho^{(1)}(n,\mathbf{q},\epsilon;n',\mathbf{q},\epsilon)$ and $\rho^{(1)}(n'',\mathbf{q}',\epsilon';n''',\mathbf{q}',\epsilon')$, where the band index pairs (n,n') and (n'',n''') are different from each other. The equations for these density matrix elements between the highly excited Bloch states can be obtained from Eq. (24) by replacing n'' with n and n''' with n'.

Second, the density matrix elements $\rho^{(1)}(n,\mathbf{q},\epsilon;n,\mathbf{q},\epsilon)$ represent a Rayleigh contribtion to the signal due to transitions beginning and ending at the same Bloch states. These density matrix elements can be obtained from Eq. (24) by replacing n' with n, n'' and n''' with n'. In calculating this part of the signal, we also include the off-diagonal density matrix elements between the Bloch states within one of the lowest energy manifolds, in which the energy separations between these states are less than their relaxations rates due to optical pumping.

In Fig. 3, an example of the Raman-type signal due to transitions between the Bloch states of different energies is shown for a potential depth $U_0 = -150E_k$. The probe-transmission spectrum is plotted against the probe-pump detuning δ/ω_k, where $\omega_k = \hbar k^2/2M$ is the recoil frequency. Similar to the 1D case, the spectrum exhibits pairs of sidebands symmetrically located at negative and positive detunings. These sidebands are dominated by the contribution due to transitions between the bound vibrational states, since the positions of these sidebands correspond approximately to the energy separations between the lower energy manifolds. The widths of the sidebands are mainly due to the spread of the Raman transition frequencies, which itself originates from the anharmonicity of the light-shift potential wells. A notable difference between the 2D spectrum shown in Fig. 3 and those of 1D molasses [7,8] is that the magnitude of the second sideband relative to that of the first sideband is greater in the 2D case than in 1D. Such a difference stems from the quasidegeneracy of the Bloch states in the 2D case, which increases with energy. For instance, the degrees of degeneracy for the first and second excited energy manifold are two and three, respectively. As a result, there are three possible transitions between the ground and the second excited manifolds that contribute to the second sideband, compared to two possible transitions between the ground and the first excited manifolds that contribute to the first sideband. As a result, the ratio between the magnitudes of the second and first sidebands becomes greater in the 2D case than in the 1D case.

In Fig. 4, we plot the Rayleigh signal, which originates from transitions beginning and ending at the Bloch states with the same energy. As can be seen from Fig. 4, the Rayleigh signal exhibits a dispersion line shape centered at $\delta = 0$, with probe amplification for $\delta < 0$ and probe absorption for $\delta > 0$, which are in qualitative agreement with some related 2D experimental results [3,4]. From Figs. 3 and 4, the calculated central signal has a magnitude much smaller than those of the Raman sidebands in the absence of probe misalignment. Such a feature is analogous to the case in 1D molasses when the probe field and the copropagating cooling field have parallel polarizations [8]. As shown in the next section, the inclusion of a small misalignment of the probe field, either in the x-y plane or in the x-z plane, can lead to significant modifications to this central Rayleigh signal.

One of the unusual features revealed in previous calculations on 2D cooling in this configuration is the existence of resonance peaks in the populations of the lowest Bloch states as the potential depth U_0 is varied [12]. It was also shown [13] that such resonances exist only in the limit of very large detuning $|\Delta|$ (on the order of 50Γ) for which the secular approximation is valid, and as $|\Delta|/\Gamma$ decreases, these resonances peaks disappear. One possible way to observe these predicted resonance features may be through the type of probe-transmission experiments investigated in this work. In Fig. 5, we plot the probe-transmission spectra for three different values of the potential depth U_0 in the vicinity of a resonance

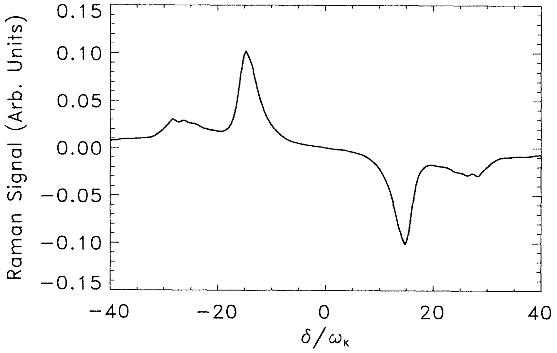

FIG. 3. Raman resonance signal. The potential depth $U_0 = -150E_k$, and the cooling field detuning $\Delta = -20\Gamma$.

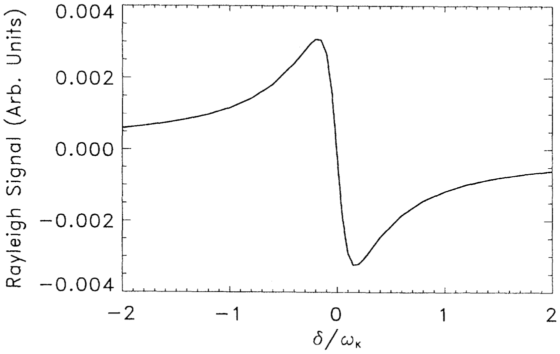

FIG. 4. Rayleigh resonance signal in the absence of probe misalignment. The cooling field parameters are the same as in Fig. 3.

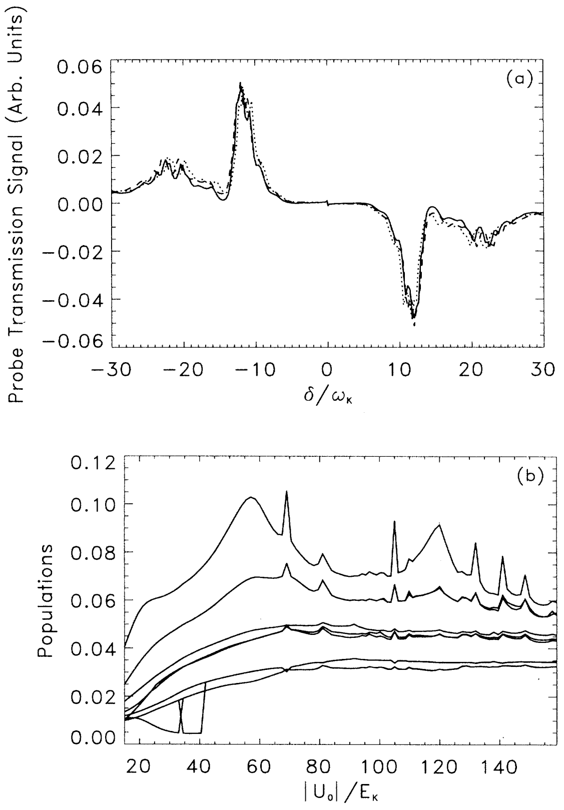

FIG. 5. (a) Probe-transmission signal in the absence of probe misalignment. The cooling field detuning $\Delta = -40\Gamma$, and the potential depth $U_0 = -102E_k$ (dotted line), $-105E_k$ (solid line), and $-108E_k$ (dashed line). (b) Populations of the lowest ten bands as a function of $|U_0|/E_k$.

peak in the population of the ground motional state. The cooling field detuning is $\Delta/\Gamma = -40$, which results in relatively narrow widths for the Raman peaks. As can be seen from Fig. 5, the differences between these spectra are small, indicating that the probe-transmission signal is insensitive to the population resonances. This is partially due to the fact that the resonance peaks in the populations are significant only for the lowest several Bloch states, whose populations are only a few percent of the total population. As a result, resonances in the lowest Bloch states do not result in any significant change in the line shape of the probe spectrum.

V. CENTRAL SIGNAL IN THE PRESENCE OF PROBE MISALIGNMENT

In the above section, we have assumed that the probe field copropagates exactly with one of the cooling field along the x axis. In reality, however, there usually exists a small angle between the directions of the probe and the cooling fields. It has been shown in a 1D case [8] that such a misalignment of the probe field can lead to significant modifications to the central signal in the probe-transmission spectrum.

In this section, we investigate the effects due to the misalignment of the probe in the 2D molasses. We consider misalignment of the probe field in the x-y plane and in the x-z plane, respectively.

A. Probe misalignment in the x-y plane

We first consider the misalignment of the probe field within the lattice plane. The probe field wave vector is assumed to be given by

$$\mathbf{k}' = k\hat{\mathbf{x}} + k\theta\hat{\mathbf{y}} \ , \tag{26}$$

where $\theta \ll 1$ is the misalignment angle. The interference between the probe and the nearly copropagating cooling field can lead to the formation of an atomic index or magnetization grating in the y direction, with a grating period given by λ/θ, where λ is the optical wavelength. For very small pump-probe detunings such that $|\delta| \ll \Gamma'$, the atomic density matrix elements representing the contribution of this grating to the signal are of the form $\rho^{(1)}(n, \mathbf{q}, \epsilon; n, \mathbf{q} + \theta k\hat{\mathbf{y}}, \epsilon)$. Similar to Eq. (24), the equations for these density matrix elements can be derived from Eq. (21) as

$$\begin{aligned}
&-[\tfrac{1}{2}(\gamma_{n,\mathbf{q},\epsilon} + \gamma_{n,\mathbf{q}+\theta k\hat{\mathbf{y}},\epsilon}) + i\delta + i\omega_{n,\mathbf{q},\epsilon;n,\mathbf{q}+\theta k\hat{\mathbf{y}},\epsilon}]\rho^{(1)}(n, \mathbf{q}, \epsilon; n, \mathbf{q} + \theta k\hat{\mathbf{y}}, \epsilon) \\
&\qquad +\Gamma' \sum_{n',\mathbf{q}',\epsilon'} \int \sum_{Q} N_Q(\mathbf{p}') \langle n, \mathbf{q}, \epsilon | (B_Q^{(0)})^\dagger e^{-i\mathbf{p}'\cdot\mathbf{r}} | n', \mathbf{q}', \epsilon' \rangle \\
&\qquad \times \langle n', \mathbf{q}' + \theta k\hat{\mathbf{y}}, \epsilon' | e^{i\mathbf{p}'\cdot\mathbf{r}} B_Q^{(0)} | n, \mathbf{q} + \theta k\hat{\mathbf{y}}, \epsilon \rangle \rho^{(1)}(n', \mathbf{q}', \epsilon'; n', \mathbf{q}' + \theta k\hat{\mathbf{y}}, \epsilon') \\
&\qquad\qquad = \frac{i}{\hbar} \langle n, \mathbf{q}, \epsilon | H^{(1)} | n, \mathbf{q} + \theta k\hat{\mathbf{y}}, \epsilon \rangle (\pi_{n,\mathbf{q}+\theta k\hat{\mathbf{y}},\epsilon} - \pi_{n,\mathbf{q},\epsilon}) + \frac{\Gamma'}{2} \langle n, \mathbf{q}, \epsilon | A^{(1)} | n, \mathbf{q} + \theta k\hat{\mathbf{y}}, \epsilon \rangle \\
&\qquad\qquad \times (\pi_{n,\mathbf{q},\epsilon} + \pi_{n,\mathbf{q}+\theta k\hat{\mathbf{y}},\epsilon}) - \Gamma' \sum_{n',\mathbf{q}',\epsilon'} \int d\mathbf{p}' \sum_{Q} N_Q(\mathbf{p}') \langle n, \mathbf{q}, \epsilon | (B_Q^{(0)})^\dagger e^{-i\mathbf{p}'\cdot\mathbf{r}} | n', \mathbf{q}', \epsilon' \rangle \\
&\qquad\qquad \times \langle n', \mathbf{q}', \epsilon' | e^{i\mathbf{p}'\cdot\mathbf{r}} B_Q^{(1)} | n, \mathbf{q} + \theta k\hat{\mathbf{y}}, \epsilon \rangle \pi_{n',\mathbf{q}',\epsilon'} \ .
\end{aligned} \tag{27}$$

As can be seen from the above equation, in order to solve these first-order density matrix elements, one needs to choose the Bloch vectors in a way such that the difference between the y component of adjacent Bloch vectors, Δq_y, satisfies

$$\Delta q_y \leq \theta k \, . \tag{28}$$

For a small value of θ, this requirement can result in a large increase in the size of atomic density matrix and the computational demands. In the calculation below, we assume a misalignment angle $\theta = 0.2$ rad, and the Bloch vectors are chosen correspondingly as

$$\mathbf{q} = (-1 + j\theta)k\hat{\mathbf{y}}, \;\; j = 0\,, 1\,, \ldots\,, 9\, . \tag{29}$$

The spontaneous emission kernels $N_Q(\mathbf{p}')$ in Eq. (8) must be discretized in accordance with the above choice of Bloch vectors, such that Eq. (27) represents a closed set of equations for the density matrix elements. In the Appendix, a possible scheme for the discretization of $N_Q(\mathbf{p}')$ is shown. Despite the different selections of the Bloch vectors in this and the previous sections, it is found that the zeroth-order atomic populations in various energy bands are within a few percent of each other in these two cases, and one expects the calculated Raman-type signals in the present case are also similar to those displayed in the previous section.

Figure 6 shows the central part of the probe-transmission signal in the presence of probe misalignment for a detuning $\Delta/\Gamma = -20$, and a potential depth $U_0/E_k = -150$. As can be seen from Fig. 6, the amplitude of the central signal is greater than the case of no misalignment shown in Fig. 4, and comparable to those of the Raman sidebands. In the presence of probe misalignment, there exist intraband Raman resonances between the Bloch states $|n, \mathbf{q}, \epsilon\rangle$ and $|n, \mathbf{q} + \theta k\hat{\mathbf{y}}, \epsilon\rangle$ involving the probe field. The contribution of these Raman resonances to the signal is partially represented by the source term proportional to $H^{(1)}$ in Eq. (27), which vanishes in the absence of probe misalignment. Moreover, a special feature in the absence of probe misalignment is that, the summation of the source terms proportional to $A^{(1)}$ exactly cancels the summation of those proportional to $B_Q^{(1)}$ in Eq. (27), as can be verified from Eqs. (11) and (12). In the presence of probe misalignment, such a feature no longer exists, and the contribution of these nonsecular terms proportional to $A^{(1)}$ and $B_Q^{(1)}$ becomes more important. These effects introduced by the misalignment of the probe field result in the observed increase in the amplitude of the central resonance signal.

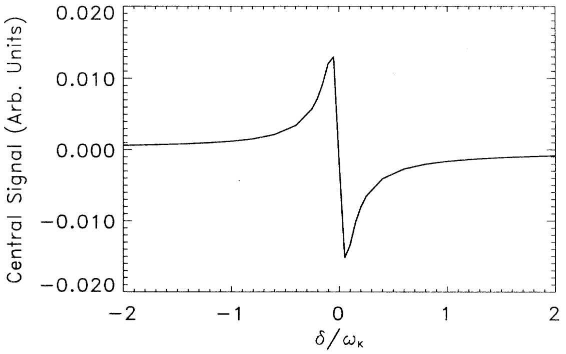

FIG. 6. Central signal in the presence of probe misalignment in the x-y plane. The cooling field parameters are the same as in Fig. 3.

B. Probe misalignment in the x-z plane: recoil-induced resonances

We next analyze the effects of the misalignment of the probe field in the x-z plane, which was the case of an earlier experiment in a 2D optical lattice described in Ref. [3]. The probe propagation direction is given by

$$\mathbf{k}' = k\hat{\mathbf{x}} - k\theta\hat{\mathbf{z}}\, , \tag{30}$$

where $\theta \ll 1$. This case is very similar to probe transmission in 1D molasses with the inclusion of probe misalignment [8]. In the 1D case, the atomic motion transverse to the molasses can be described by free-particle states (plane waves). When a probe field propagates at a small angle with a cooling field having parallel polarizations, the coherences between atomic states with their transverse center-of-mass momenta differing by $\hbar k\theta$ can be created when an atom absorbs a probe photon and emits a pump photon or vice versa. Such recoil-induced resonances (RIR) [17,18] have been shown to lead to additional contribution to the central probe-transmission signal in certain cases [8]. In the present 2D lattice with a probe misalignment in the x-z plane, one finds a similar situation where the recoil-induced resonances are expected to contribute to the central signal, since the atomic motion along the z direction can be described by free-particle states as well.

The equation for the atomic density matrix elements representing the recoil-induced signal can be derived in almost exactly the same way as in the 1D case, and the details of the derivation can be found in Ref. [8]. Including the atomic motion in the z direction, which is described by the momentum eigenstates $|p_z\rangle$, the atomic density matrix elements can be written as

$$\rho_{n,\mathbf{q}',\epsilon;n',\mathbf{q}',\epsilon'}(p_z, p_z') = \langle p_z|\langle n, \mathbf{q}, \epsilon|\rho|n', \mathbf{q}', \epsilon'\rangle|p_z'\rangle\, . \tag{31}$$

The first-order coherences between the atomic states with different center-of-mass momenta in the z direction, which represent the recoil-induced signal, is given by

$$\rho^{(1)}(p_z, p_z - \hbar k\theta) = \sum_{n,\mathbf{q},\epsilon} \rho^{(1)}_{n,\mathbf{q},\epsilon;n,\mathbf{q},\epsilon} \times (p_z, p_z - \hbar k\theta)\, . \tag{32}$$

In the secular limit ( ), the equation for $\rho^{(1)}(p_z, p_z - \hbar k\theta)$ can be shown to be given by

$$\dot{\rho}^{(1)}(p_z, p_z - \hbar k\theta) = -\left(i\delta + i\frac{kp_z\theta}{M}\right)\rho^{(1)}(p_z, p_z - \hbar k\theta) + \frac{i}{\hbar}\left[\sum_{n,\mathbf{q},\epsilon}\langle n, \mathbf{q}, \epsilon|H^{(1)}|n, \mathbf{q}, \epsilon\rangle\pi_{n,\mathbf{q},\epsilon}\right] \times [W(p_z) - W(p_z - \hbar k\theta)]\, , \tag{33}$$

where $W(p_z)$ is the atomic momentum distribution function in the z direction, which is assumed to have a typical width given by $p_0 = Mu$, where u is the most probable atomic speed in the z direction. The solution for $\rho^{(1)}(p_z, p_z - \hbar k\theta)$ in a long-time limit ($ku\theta t \gg 1$) can be obtained from Eq. (33), and upon substitution of this solution into Eq. (14), one finds the recoil-induced probe transmission signal as

$$\begin{aligned} G_P^{(\mathrm{RIR})} &= \mathrm{Im}\left[\frac{\chi}{i\Gamma/2 - \Delta}\int \rho^{(1)}(p_z, p_z - \hbar k\theta)dp_z\right] \\ &= \mathrm{Im}\left\{\frac{\pi\chi M U_0}{6(\Gamma/2 + i\Delta)}W'\left(-\frac{M\delta}{k\theta}\right)\left[1 + \sum_{n,\mathbf{q},\epsilon}\langle n,\mathbf{q},\epsilon|e^{-2ikx}|n,\mathbf{q},\epsilon\rangle\pi_{n,\mathbf{q},\epsilon}\right.\right. \\ &\quad \left.\left. + \sum_{n,\mathbf{q}}[\langle n,\mathbf{q},+|\cos(ky)e^{-ikx}|n,\mathbf{q},+\rangle\pi_{n,\mathbf{q},+} - \langle n,\mathbf{q},-|\cos(ky)e^{-ikx}|n,\mathbf{q},-\rangle\pi_{n,\mathbf{q},-}]\right]\right\}, \end{aligned} \tag{34}$$

where $W'(p_z)$ is the first-order derivative of $W(p_z)$ with respect to p_z. For a Maxwellian distribution

$$W(p_z) = \frac{1}{\sqrt{\pi}p_0}e^{-p_z^2/p_0^2}, \tag{35}$$

one obtains a typical line shape for the recoil-induced signal as

$$G_p^{(\mathrm{RIR})} \propto \frac{U_0}{k_B T_z}\frac{\delta}{ku\theta}\exp\left[-\frac{\delta^2}{(ku\theta)^2}\right], \tag{36}$$

where $k_B T_z = Mu^2/2$ is the average kinetic energy of the atomic motion along the z direction. As in the 1D case [8], the recoil-induced signal exhibits a Gaussian-type dispersion profile, with a width given by the residual Doppler width $ku\theta$, and a magnitude inversely proportional to the temperature $k_B T_z$. In Fig. 7, the signal given by Eq. (34) is plotted for a kinetic energy $k_B T_z = 100E_k$, and a misalignment angle $\theta = 0.05$ rad. The parameters for the cooling field are the same as in Figs. 3 and 4. Comparing Figs. 4 and 7, it can be seen that for the chosen temperature T_z, which is typical of sub-Doppler cooling, the recoil-induced signal can be much greater in magnitude than the Rayleigh signal in the absence of probe misalignment.

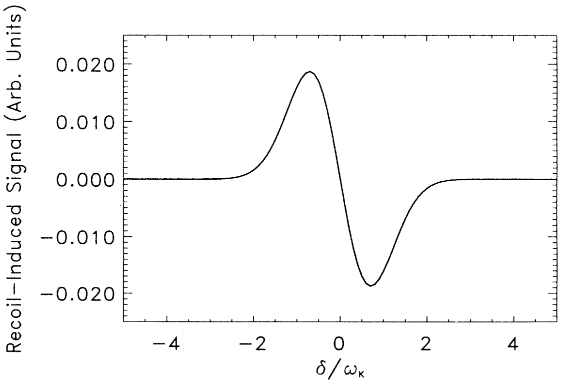

FIG. 7. Recoil-induced signal. The temperature T_z is given by $k_B T_z = 100E_k$, and the misalignment angle in the x-z plane is $\theta = 0.05$ rad. Other parameters are the same as in Fig. 3.

VI. CONCLUSIONS

In this paper we have presented a calculation of the probe-transmission spectrum of a 2D optical lattice. The atomic internal level scheme is chosen as a $J_g = 1/2 \to J_e = 3/2$ transition for simplicity, and the atomic center-of-mass motion is quantized in this calculation. The calculated spectrum exhibits both sidebands and central resonance structures, which can be explained based on stimulated Raman and Rayleigh transitions between the eigenstates of the atomic motion in the light-induced potentials. The Rayleigh signal exhibits a dispersion line shape centered at $\delta = 0$, while the Raman sidebands occur at detunings corresponding to the energy differences between the motional eigenstates.

We have also included in this calculation the misalignment of the probe field, both inside and outside of the 2D molasses plane (x-y plane). In the case of misalignment in the x-y plane, we have found that the magnitude of the central resonance signal increases as a result of the probe misalignment, which can be partially explained by the Raman intraband resonances between the Bloch states having different Bloch indices. In the case of probe misalignment in the x-z plane, the recoil-induced resonances between the free-particle states along the z direction becomes important, which lead to an additional signal at $\delta = 0$ with a Gaussian-type dispersion profile, and a width proportional to the misalignment angle θ.

The experiments on 2D probe transmission have been carried out, with both a field configuration investigated in this calculation [3] and a three-beam configuration described in Ref. [4]. In the former case, the probe field propagates with a small misalignment in the x-z plane, similar to the case studied in Sec. V B. The observed spectral features, such as relative magnitudes and line shapes of exhibited structures, are in qualitative agreement with this calculation. A recent four-wave mixing experiment on a 3D lattice has studied the effects of probe misalignment within the x-y plane [6], and it was found that the width of the central resonance signal also depends on the misalignment angle. In the present calculation, we have chosen a relatively large misalignment angle $\theta = 0.2$ rad in the x-y plane. Due to limited computing resources, we have not been able to study the cases of smaller values of θ, and therefore the dependence of the signal amplitude and width on θ in this 2D case, although numerical calculations can be performed in the same fashion as described in Sec. V A. Investigation on the angle dependence, with a generalization to 3D lattices, will be the subject of future research.

ACKNOWLEDGMENTS

I wish to thank K. Berg-Sørensen for many helpful discussions. This research was supported by the E. U. Condon Fellowship at JILA.

APPENDIX

In this appendix, we describe two different discretization schemes for the spontaneous emission kernels $N_Q(\mathbf{p}')$ used in Secs. IV and V. Our starting point is the analytical formula for the feeding term of the atomic ground state from the excited states due to spontaneous emission, as is derived in detail in Ref. [13]. In this 2D case, the feeding term can be written as

$$\begin{aligned}[\dot{\rho}_{gg}]_{\mathrm{relax}} = \frac{3\Gamma}{4\pi} \int d^2\mathbf{n}_\perp \frac{1}{\sqrt{1-\mathbf{n}_\perp^2}} e^{-ik\mathbf{n}_\perp\cdot\mathbf{r}} &\times \Bigg[\sum_{i=x,y,z} \sigma_{ge}^{(i)} \rho_{ee} \sigma_{eg}^{(i)} \\ &- (\boldsymbol{\sigma}_{ge}\cdot\mathbf{n}_\perp)\rho_{ee}(\boldsymbol{\sigma}_{eg}\cdot\mathbf{n}_\perp) \\ &- (1-\mathbf{n}_\perp^2)\sigma_{ge}^{(z)}\rho_{ee}\sigma_{eg}^{(z)} \Bigg] e^{ik\mathbf{n}_\perp\cdot\mathbf{r}} , \qquad \text{(A1)}\end{aligned}$$

where in Cartesian coordinates, $\mathbf{n}_\perp = (\sin\alpha\cos\beta, \sin\alpha\sin\beta, 0)$, and (α,β) are the polar angles. In Eq. (A1), $\boldsymbol{\sigma}_{eg}$ ($\boldsymbol{\sigma}_{ge}$) are the atomic raising (lowering) operators, whose spherical components for the $J_g = 1/2 \rightarrow J_e = 3/2$ transition are given by

$$\begin{aligned}\sigma_{eg}^{(\pm1)} &= |e \pm 3/2\rangle \bigg\langle g \pm 1/2| \\ &\quad + \frac{1}{\sqrt{3}} |e \pm 1/2 \bigg\rangle \langle g \mp 1/2| , \\ \sigma_{eg}^{(0)} &= \sqrt{\frac{2}{3}} (|e1/2\rangle\langle g1/2| + |e-1/2\rangle\langle g-1/2|) . \qquad \text{(A2)}\end{aligned}$$

The atomic excited-state density matrix ρ_{ee} in Eq. (A1) can be expressed in terms of ρ_{gg} as

$$\rho_{ee} = [\boldsymbol{\sigma}_{eg}\cdot\boldsymbol{\epsilon}(\mathbf{r})]\rho_{gg}[\boldsymbol{\sigma}_{ge}\cdot\boldsymbol{\epsilon}^*(\mathbf{r})] , \qquad \text{(A3)}$$

where $\boldsymbol{\epsilon}(\mathbf{r})$ is the polarization vector of the incident field.

For the purpose of numerical calculation, one needs to discretize the Bloch index $\mathbf{q}$ as well as the spontaneous emission kernel in Eq. (A1). Our criterion for choosing the discretization schemes are mainly based on minimizing the numerical computation. In the absence of probe misalignment, or in the presence of a small probe misalignment in the x-z plane, one can choose the Bloch indices given by Eq. (23). The simplest spontaneous emission pattern compatible with this choice of $\mathbf{q}$ is to assume that the fluorescence photons are emitted only along the Cartesian axes x, y, z. As a result, Eq. (A1) becomes [13]

$$\begin{aligned}[\dot{\rho}_{gg}]_{\mathrm{relax}} = \frac{\Gamma}{4} \sum_{\eta=\pm} \sum_{m=x,y,z} \sum_{l\neq m} &\times \sigma_{ge}^{(m)} e^{-ikr_l\eta} \rho_{ee} e^{ikr_l\eta} \sigma_{eg}^{(m)} , \qquad \text{(A4)}\end{aligned}$$

or, in terms of the spontaneous emission kernels $N_Q(\mathbf{p}')$ in Eq. (8),

$$\begin{aligned}N_{\pm1}(\mathbf{p}') &= \frac{1}{8}[\delta(\mathbf{p}'-k\hat{\mathbf{x}}) + \delta(\mathbf{p}'+k\hat{\mathbf{x}}) \\ &\quad + \delta(\mathbf{p}'-k\hat{\mathbf{y}}) + \delta(\mathbf{p}'+k\hat{\mathbf{y}}) + 4\delta(\mathbf{p}')] , \\ N_0(\mathbf{p}') &= \frac{1}{4}[\delta(\mathbf{p}'-k\hat{\mathbf{x}}) + \delta(\mathbf{p}'+k\hat{\mathbf{x}}) \\ &\quad + \delta(\mathbf{p}'-k\hat{\mathbf{y}}) + \delta(\mathbf{p}'+k\hat{\mathbf{y}})] . \qquad \text{(A5)}\end{aligned}$$

In the presence of a small probe misalignment in the x-y plane, the interval between different Bloch vectors must be sufficiently small to resolve the probe-induced grating structure. For the choice of Bloch vectors described in Eq. (29), the azimuthal angle β can be chosen such that the projection of the fluorescence photon momentum in the x-y plane is along the x or y axis only, i.e., $\beta = 0, \pi/2, \pi, 3\pi/2$. For the case of $\beta = 0$ or π, the spontaneous photon wave vectors can be assumed to be in the x direction only, i.e.,

$$\mathbf{n}_\perp k = \pm k\hat{\mathbf{x}} \quad \text{for } \beta = 0, \pi . \qquad \text{(A6)}$$

For $\beta = \pi/2$ or $3\pi/2$, $\mathbf{n}_\perp$ is discretized as follows:

$$\begin{aligned}&\mathbf{n}_\perp k = (-k + j\theta k)\hat{\mathbf{y}}, \\ &j = 0, 1, \ldots, 2/\theta , \quad \text{for } \beta = \pi/2, 3\pi/2 . \qquad \text{(A7)}\end{aligned}$$

The probabilities associated with each fluorescence photon momentum can be derived from Eq. (A1). Based on a direct discretization of the integral in Eq. (A1), we obtain the spontaneous emission kernels $N_Q(\mathbf{p}')$ as follows:

$$\begin{aligned}N_{\pm1}(\mathbf{p}') &= \frac{1}{8}[\delta(\mathbf{p}'-k\hat{\mathbf{x}}) + \delta(\mathbf{p}'+k\hat{\mathbf{x}}) + 2\delta(\mathbf{p}')] \\ &\quad + \sum_{j=0}^{2/\theta} P_{\pm1}(p(j))\delta(\mathbf{p}' - p(j)\hat{\mathbf{y}}) , \\ N_0(\mathbf{p}') &= \frac{1}{4}[\delta(\mathbf{p}'-k\hat{\mathbf{x}}) + \delta(\mathbf{p}'+k\hat{\mathbf{x}})] \\ &\quad + \sum_{j=0}^{2/\theta} P_0(p(j))\delta(\mathbf{p}' - p(j)\hat{\mathbf{y}}) , \qquad \text{(A8)}\end{aligned}$$

where

$$p(j) = (-1 + j\theta)k , \qquad \text{(A9)}$$

and

$$P_{\pm1}(p(j)) = \frac{3}{16}\left[\frac{|p(j)|}{\sqrt{1-p(j)^2}} + 1.1|p(j)|\sqrt{1-p(j)^2}\right] , \quad j \neq 0\,,2/\theta \,,$$
$$P_{\pm1}(p(j)) = 0.085 \,, \quad j = 0\,,2/\theta \,,$$
$$P_0(p(j)) = \frac{3}{8}\frac{|p(j)|^3}{\sqrt{1-p(j)^2}} \,, \quad j \neq 0\,,2/\theta \,,$$
$$P_0(p(j)) = 0.16 \,, \quad j = 0\,,2/\theta \,. \tag{A10}$$

The kernels $N_Q(\mathbf{p}')$ shown above satisfy the normalization conditions $\sum_{\mathbf{p}'} N_Q(\mathbf{p}') = 1$ for $Q = \pm1, 0$, respectively.

[1] P. Verkerk, B. Lounis, C. Salomon, C. Cohen-Tannoudji, J.-Y. Courtois, and G. Grynberg, Phys. Rev. Lett. **68**, 3861 (1992).

[2] P. Jessen, C. Gerz, P. D. Lett, W. D. Phillips, S. L. Rolston, R. J. C. Spreeuw, and C. I. Westbrook, Phys. Rev. Lett. **69**, 49 (1992).

[3] A. Hemmerich and T. W. Hänsch, Phys. Rev. Lett. **70**, 410 (1993).

[4] G. Grynberg, B. Lounis, P. Verkerk, J.-Y. Courtois, and C. Salomon, Phys. Rev. Lett. **70**, 2249 (1993).

[5] A. Hemmerich, C. Zimmermann, and T. Hänsch, Phys. Rev. Lett. **72**, 625 (1994).

[6] A. Hemmerich, M. Weidemüller, and T. Hänsch, Europhys. Lett. **27**, 427 (1994).

[7] J.-Y. Courtois and G. Grynberg, Phys. Rev. A **46**, 7060 (1992).

[8] J. Guo, Phys. Rev. A **49**, 3934 (1994); **51**, 2338 (1995).

[9] K. Mølmer, Phys. Rev. A **44**, 5820 (1991).

[10] J. Javanainen, Phys. Rev. A **46**, 5819 (1992).

[11] V. Finkelstein, J. Guo, and P. R. Berman, Phys. Rev. A **46**, 7180 (1992).

[12] K. Berg-Sørensen, Y. Castin, K. Mølmer, and J. Dalibard, Europhys. Lett. **22**, 663 (1993).

[13] Y. Casin, K. Berg-Sørensen, J. Dalibard, and K. Mølmer, Phys. Rev. A **50**, 5092 (1994).

[14] A greater value of $N_{\rm max}$ may be chosen as well with increased numerical computation, but we expect the qualitative features of the calculated spectrum to be similar.

[15] Y. Castin and J. Dalibard, Europhys. Lett. **14**, 761 (1991).

[16] J. Guo and P. R. Berman, Phys. Rev. A **48**, 3225 (1993).

[17] J. Guo, P. R. Berman, B. Dubetsky, and G. Grynberg, Phys. Rev. A **46**, 1426 (1992).

[18] J.-Y. Courtois, G. Grynberg, B. Lounis, and P. Verkerk, Phys. Rev. Lett. **72**, 3017 (1994).